비선형 hydromechanic 효과를 고려한 이산 균열망 모형에서의 유체흐름과 오염물질 이송에 관한 수치모의 실험

Fluid Flow and Solute Transport in a Discrete Fracture Network Model with Nonlinear Hydromechanical Effect

정 우 창[*] / 송 재 우[**]

Jeong, Woo Chang / Song, Jai Woo

Abstract

Numerical simulations for fluid flow and solute transport in a fracture rock masses are performed by using a transient flow model, which is based on the three-dimensional stochastic and discrete fracture network model (DFN model) and is coupled hydraulic model with mechanical model. In the numerical simulations of the solute transport, we used to the particle following algorithm which is similar to an advective biased random walk. The purpose of this study is to predict the response of the tracer test between two deep bore holes (GPK1 and GPK 2) implanted at Soultz sous Forët in France, in the context of the geothermal researches. The data sets used are obtained from in situ circulating experiments during 1995. As the result of the transport simulation, the mean transit time for the non reactive particles is about 5 days between two bore holes.

Keywords : fracture network, effective normal stress, Mohr-Coulomb criterion, mean transit time

요 지

균열 암반 매질에서의 지하수 흐름과 오염물질 이송에 대한 수치모의 실험이 hydromechanic 모형과 추계적 그리고 이산적 3차원 균열망 모형에 바탕을 둔 비정상상태 흐름 수치 모형을 이용하여 수행되었다. 오염물질 이송에 대한 수치모의 실험에서 random walk의 일종인 particle following 알고리즘이 사용되었다. 이 연구의 목적은 지하 깊은 곳에 위치한 Hot dry rock에서의 지열 개발을 위해 프랑스 Soultz sous Forët 지역에 설치된 두 개의 깊은 착정인 GPK1과 GPK2 사이에서의 tracer test 반응을 1995년에 실행된 유체순환 현장 실험으로부터 얻어진 자료를 이용하여 예측하는 것이다. 모의 실험 결과 비반응입자(nonreactive particles)에 대한 평균 이송시간은 두 착정 사이에서 약 5일 이었다.

핵심용어 : 균열망, 유효수직응력, 모어-쿨롱규준, 평균이송시간

---

[*] Post-graduate course in Ecole des Mines de Paris
[**] 홍익대학교 토목공학과 교수

1. Introduction

The study for the hydraulic behaviours in the hard rock masses has been considered as an important domain, particularly for the potential disposal sites of radioactive wastes and the hot dry rock (HDR) geothermal resources. The permeabilities in these mediums are in general very low but because of the existence of the faults and the fractures created by the tectonic forces, these mediums cannot be regarded as impervious geological barriers for flow.

The fractured rock masses are significantly heterogeneous and when they are sparsely and weakly connected, the averaging volume necessary to obtain their representativ elemental volume could be much larger than the scale of interest. At the laboratory scale with a single fracture, studies indicate that there is a large variation in the asperities and in the apertures on a fracture surface and fluid flows along preferential tortuous channels of varying the hydraulic properties (Gentier S.,1986; Moreno et al., 1988). At an intermediate scale, the fluid flow is driven not only by the hydraulic conductivity of fractures but also by their connectivity to the rest of the fracture network. This is clearly shown by the hydraulic tests between packers performed along the bore holes (Bruel et al., 1994). At a large scale which is the scale of the circulated system, dominant structures including fracture zones or faults may govern the global flow and have to be located andidentified in near vicinity of the site characterization program. With regard to these hydraulic behaviours, the discrete fracture network models have been developed (Andersson and Dverstrop, 1987; Cacas et al., 1990; Nordqvist et al., 1992).

The objective of this study is to simulate numerically the fluid flow and the tracer test prediction with the transient three-dimensional discrete fracture network model using the data sets obtained from the forced circulating experiments performed between two deep bore holes GPK 1 and GPK 2 implanted at Soultz sous Fort in France, for the purpose of the geothermal exploitation researches in such fractured medium.

2. Basic Description of Modelling Approach

2.1 Geometrical Model

In this modelling approach which is derived from Cacas et al. (1990), the properties of individual fractures are randomly and independently generated in a three-dimensional volume, as portion of plans with available measured statistics of the physical fracture network (*i.e.* fracture density, orientation distribution for each fracture set and fracture size distribution). The shape of these fracture elements is assumed to be disc-shaped such as in the Baecher model (Baecher et al., 1977).

The number of fracture centers is generated by Poisson process. The orientation of each fracture is defined by its normal vector which

Fig. 1. An example of the fracture network in 3-D space

is derived from a truncated Fisher von Mises distribution function and the extension of the fractures is characterized by their radii which are generated by a log-normal distribution function. The parameters of these distribution functions are determined by the statistical analysis of data obtained from outcrops, drifts or bore hole cores. Fig. 1 is illustrated as an example of fracture network generated in 3-D space.

2.2 Local Fluid Flow Model Combined with the Compliance Effect

According to the Cacas' approach (1990), the fluid flow occurs only in the fracture network. Therefore, the fluid migration from the fracture into rock matrix is not considered. The fluid flow model assumes that each fracture contains 1-D flow channel linking the centers of adjacent fracture elements (Fig. 2).

In general, the amount of the fluid flow passing through a fracture is a function of the aperture cubed (Gale, 1982). This relationship,
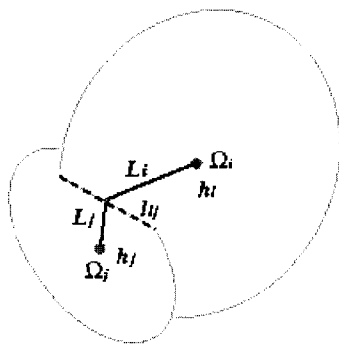

Fig. 2. Ω_i and Ω_j are the centers of two connected fracture elements. l_{ij} is the width of their intersection (dash line). L_i and L_j are the distances between each i and j fractures and mid-point of intersected segment (solid line). h_i and h_j are respectively the hydraulic heads at two fracture centers i and j.

referred to as the cubic law, is valid in describing flow through the fractures having a constant aperture distribution (Gale et al., 1985). However, the significant deviation from this general behaviour takes place when applying the stress in the fractured medium (Gale, 1982; Raven and Gale, 1985). This discrepancy is actually attributed to the changes in the morphological aspects of the fracture surface (i.e. spatial distribution of apertures in contact, disconnected voids and tortuosity) and the fact that the flow occurs on the limited number of channels, known as channelling effect (Gentier, 1986; Tsang et al., 1988). To be consistent with this channelling evidence within the fracture surface, and because in situ measurements of the fracture apertures and morphological description are most of the time not reliable, the hydraulic properties are considered as parameters.

In order to represent the hydraulic effects of compliance mentioned above, a simplified but a realistic nonlinear relationship between the hydraulic conductivity and stress is used (Bruel et al., 1994). Here, the hydraulic conductivity at any stress level can be defined by the hydraulic conductivity at zero effective normal stress k_0 times a given efficiency factor which depends on the stress. For a fracture element i (Fig. 2), the hydraulic conductivity at zero effective normal stress k_{0i} is given by:

$$k_{0i} = \frac{l_{ij}\, g\, e_{0i}^3}{12\nu} \tag{1}$$

where l_{ij} is the intersected width between two interconnected fractures i and j, e_{0i} is the aperture of fracture i at zero effective normal stress level and ν and g are the kinematic viscosity and the gravitational acceleration respectively. The efficiency factor corresponds to the compliance effect in a rough walled fracture where the areas in contact are enlarged

while the effective normal stress is increased. In order to define this factor, the following two analytical formulae can be used.

2.2.1 Relation of the Change in Stress to the Change in Void Space, τ

Let define τ being the ratio of the void space per unit area as a function of the normal loading stress σ and of the fluid pressure Ψ. This is expressed as an exponential function increasing from a minimum value τ_0 up to the maximum level unity, as follows:

$$\tau = \tau_0 + (1 - \tau_0) \exp\left[\left(\frac{\sigma - \Psi}{\beta} \right)^q \right] \qquad (2)$$

where β is an empirical constant expressed in MPa and $q > 1$ is an empirical shape factor. This function is not permitted to apply the fluid pressure Ψ larger than normal loading stress σ. The effective normal stress $(\sigma - \Psi)$ is computed at each disc center, as would be done for a single penny shape fracture, ignoring the effects of mechanical interactions between fractures. The far field stress tensor σ, the normal vector of the fracture n and the fluid pressure Ψ are combined to produce the resolved stress component $\overline{\sigma}$ as follows:

$$\overline{\sigma} = \sigma n \cdot n - \Psi \qquad (3)$$

2.2.2 Relation of the Change of the Area in Contact to the Change of the Hydraulic Conductivity, $f(t)$

This relationship reflects the effect of tortuosity which increases while t decreases toward a limiting value τ_∞. The hydraulic conductivity is set to $k_i = f(\tau) \times k_{0i}$ which is equivalent to the hydraulic conductivity of a channel with an efficient width $l_{ij}(\sigma)(= f(\tau) \times l_{ij})$ for fluid flow. This
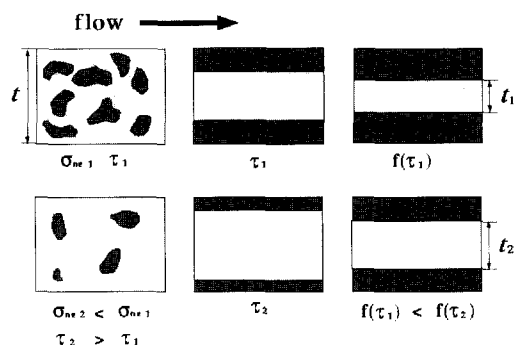

Fig. 3. Equivalent hydraulic properties of a given bond flow path, at two different effective normal stress levels, σ_1' and σ_2'. Equivalent width l_1 and l_2 of the 1-D bonds of aperture e_0. The dark areas on the left figure represent the areas in contact.

relationship is also given by an exponential function as follows:

$$f(\tau) = \exp[-\alpha(1 - \tau)^r] \qquad (4)$$

Eqn. (4) allows the different behaviour with a limited number of the free parameters (*i.e.* $a > 0$ and $r > 0$), ensuring the positive values of $f(\tau)$ for the entire range of $\tau \in [0, 1]$. The graphical description of this non-linear behaviour relative to the two analytical functions mentioned above is presented in Fig. 3.

2.3. Model for Stimulation Effects

The stimulations are the hydraulic treatments with high fluid pressures and flow rate levels and allow the various mechanical processes to occur and interact along the fracture planes, according to the spatial stress distribution.

For each fracture element, the effective normal stress $\sigma'(= \sigma - \Psi)$ and the supported shear stress s can be calculated from its location, its orientation and from the far field principal stresses. Assuming a uniform stimulation pressure Ψ within the stimulated rock volume, reduced effective normal stresses

are derived at each fracture center. Following a simple Mohr-Coulomb criterion, the amount of shear stress Δs released in non stable conditions is calculated and for tensile displacements the shear stress is reduced to zero.

$$\Delta s = C - \sigma' \tan(\Phi) \tag{5}$$

where C is the cohesion expressed in MPa and Φ is the internal friction angle.

In our model, this excess of the shear stress is then converted into a slip displacement Δu which is evaluated at each stimulated fracture element by the following equation:

$$\Delta u = 4 \frac{1 - \nu^2}{1 - \nu} \frac{\Delta s}{E} r \tag{6}$$

where E is the Young's modulus, ν is the Poisson ratio of the elastic rock mass surrounding a fracture and r is the fracture element radius.

According to a dilatant effect owing to the expected roughness of the fracture walls, this tangential displacement is turned into a normal displacement Δe which is increased to the assigned aperture at zero effective normal stress e_0. For a given fracture, we assume that the normal displacement Δe can not excess the limiting value e_0, which is very rough approach for reproducing the final effect of the fracture surface damages occuring during the sliding motion.

$$\Delta e = \min \ (e_0 \cdot \tan(\alpha) \times \Delta u) \tag{7}$$

where α is the dilatancy angle.

For further computations with the pressure levels lower than the stimulation pressure, the compliance effect applies to these updated values $e_0 + \Delta e$ of the apertures.

3. Steady-state and Transient Flow

We assume that the flow is always in laminar range and that the cubic law is locally valid, at the scale of a fracture element, which behaves as a pair of parallel smooth plates. Let k_i and k_j represent the hydraulic conductivity of two connected channels in fractures i and j, as illustrated in Fig. 2. L_i and L_j are the different channel lengths respectively used in the calculation of volumetric flux q_{ij} established between two fracture elements i and j where the difference of the hydraulic head is $h_i - h_j$.

The flux q_{ij} between two fracture elements i and j is proportional to the hydraulic head gradient and is evaluated by the following equation:

$$q_{ij} = k_{ij} \frac{h_i - h_j}{L_i + L_j} \tag{8}$$

where k_{ij} is the harmonic mean of k_i and k_j defined by

$$k_{ij} = \frac{k_i k_j (L_i + L_j)}{k_j L_i + L_j k_i} \tag{9}$$

In steady-state flow model, the calculation of the global flow rate through entire fracture network is carried out by applying the principle of the mass conservation. If the n_i different fracture elements j are connected at each fracture i, it follows from the mass balance as follows:

$$\sum_{j}^{n} q_{ij} = 0 \tag{10}$$

The transient flow model reflects the capacitive properties defined from the effect of morphological changes in the void distribution, owing to the variation of the effective normal stress. The local storage coefficient C_i is

calculated at each fracture i as the ratio of void change per unit change in the effective normal stress and is given by:

$$C_i = -\frac{d\tau_i}{d\sigma_i'} \tag{11}$$

We assume that each fracture i acts an inflating or deflating single reservoir and that the internal fluid pressure change is dh_i during the elapsed time dt the change in mass in each fracture is added in Eqn. (10), which is replaced by:

$$\sum_j^{n_i} q_{ij} = C_i V_i \frac{dh_i}{dt} \tag{12}$$

where $V_i (= \pi \times r_i^2 \times e_i)$ is the volume of fracture i having radius r_i and aperture e_i.

The matrix form of Eqn. (12) is given by:

$$[K]\{h\} = [C]\left\{\frac{dh}{dt}\right\} + \{b\} \tag{13}$$

where b is a vector specifying sources or sinks at particular nodes.

The linearization for the temporal derivative is obtained by a lumped formulation (Huyakorn and Pinder, 1983):

$$\left[\frac{dh}{dt}\right]_{t+a} = \frac{h(t+\varDelta t) - h(t)}{\varDelta t} \tag{14}$$

where α is the time-weighting factor and has a range of $[0., 1.]$. The standard form of Eqn. (13) is given by:

$$\left[\frac{C}{\varDelta t} - a[K]\right]\{h\}_{t+\varDelta t} =$$
$$\left[(1-a)[K] + \frac{C}{\varDelta t}\right]\{h\}_t - \{b\} \tag{15}$$

where $[K]$ and $[C]$ are evaluated at each iteration using the head values obtained by the linear interpolation over the time step.

As initial conditions, a distribution of fluid pressure corresponding to the hydrostatic

equilibrium is introduced. The hydraulic head or flux for the prescribed boundary conditions can be also used. Because of the sparse property of matrix $[K]$ due to the high heterogeneous nature of the global flow matrix, an iterative preconditionning gradient conjugate method has been implemented using an incomplete Cholesky algorithm (Ciarlet, 1988; Ezzedine, 1994).

4. Transport Model

4.1 Description of Particle Following Method

This method is similar to an advective biased random walk through the 3-D fracture network consisted of all the 1-D channel (Robinson, 1984; Cacas, 1989). This is a simplified process which allows to generate the transit time that the probabilistic density function is expressed as follows:

$$f(t) = \frac{1}{2}\left(u + \frac{x_m}{t}\right)\frac{1}{\sqrt{4\pi Dt}} \exp\left[\frac{(x_m - ut)^2}{4Dt}\right] \tag{16}$$

where x_m is the bond length, D is the coefficient of longitudinal dispersion and u is the mean velocity in a channel.

This probabilistic density function means the fact that the particles is governed by the longitudinal dispersion according to the Fick's law. The particles introduced simultaneously in a given point form a cloud which is dispersed during time and its density along the flow direction is a gaussian distribution. The standard deviation of particles at any moment depends on the coefficient of dispersion and the observation time:

$$S = \sqrt{2Dt} \tag{17}$$

The method developed is based on the following procedure. Let t_m the time taken by a particle moved according to the mean velocity u:

$$t_m = \frac{t_m}{u} \tag{18}$$

$$t = \frac{x_m}{x_m + Sa} \cdot t_m \tag{20}$$

We know that the distances displaced by a set of particles released at $t = 0$ are distributed by gaussien distribution law at t_m and its means μ and standard deviation S are expressed by:

$$\mu = x_m \qquad S = \sqrt{\text{const.} \times x_m} \tag{19}$$

This method is to do the random sampling of the position of particle x at t_m. The mean velocity of the particle between $t = 0$ and $t = t_m$ is hence deduced. Taking theapproximation that this mean velocity is constant along the bond length, the transit time t is given by:

where a is the random number in $[-1,1]$ generating according to Gaussian distribution law.

We assume that the simulated transit times are distributed as inverse of normal distribution law. The probability density function of such law is given by:

$$f(\nu) = -\frac{1}{\sigma\sqrt{2\pi\nu^2}} \exp\left[\frac{\left(\frac{1}{\nu} - m\right)^2}{2\sigma^2}\right] \tag{21}$$

where m and σ are the mean and the standard deviation of the variable $1/\nu$.

Substituting $t/x_m \times t_m$ for ν, we can obtain the following probability density function:
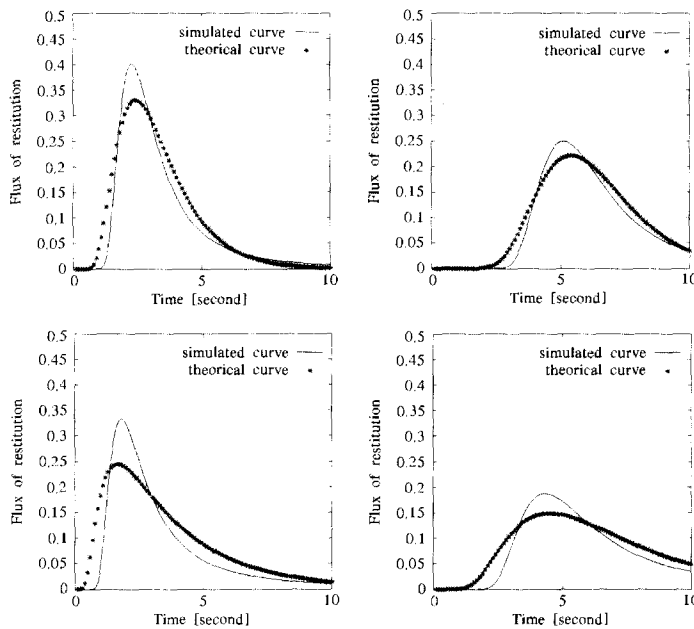

Fig. 4. Simulation of the dispersion in a 1-D channel: Comprison between two probability density functions (Top : 3 (left) and 6 (right) m of channel length with 1.0 ms^{-1} of mean velocity and 0.3 m^{2}s^{-1} of coefficient of dispersion. Bottom : 3 (left) and 6 (right) m of channel length with 1.0 ms^{-1} of mean velocity and 0.8 m^{2}s^{-1} of coefficient of dispersion.

$$f(t) = \frac{t_m}{t} \frac{x_m}{\sqrt{4\pi D t_m t}} \exp\left[- \frac{\left\{ x_m^2 \left(\frac{t_m}{t} - 1 \right)^2 \right\}}{4 D t_m} \right]$$
(22)

This function is compared with the exact probability density function as follows:

$$f(t) = \frac{1}{2}\left(\frac{t}{t_m} + 1 \right) \frac{x_m}{\sqrt{4\pi D t t}} \exp\left[\frac{x_m^2 \left(1 - \frac{t}{t_m^2} \right)}{4 D t} \right]$$
(23)

Fig. 4 shows the comparison of the results obtained between these two functions for different values of the coefficient of dispersion and different values of the channel length. It appears that the difference between two results remains completely acceptable. This difference increases when the coefficient of dispersion increases, but this diminishes when the channel length increases.

4.2 Retardation Effect due to Tortuosity and Adsorption

Particles are introduced on the up-stream boundary (*i.e.* the reinjection bore hole) and collected on the down-stream boundary (*i.e.* the production bore hole). At the fracture centers, a particle selects a new direction according to a random process weighted by the outgoing local flux. In our transport model, we assume a perfect mixing within each fracture. The transit time of a particle in each channel is directly calculated from the flux at this particular position and from the volume of this channel.

Because of the local flow model, the porosity is proportional to the open section of the channel perpendicular to the flow, that is $\tau \times l_{ij} \times e_{0i}$. As mentioned in section 2.2, the flux at each fracture center is calculated with the equivalent open section $l_{ij}(\sigma')(= f(\tau) \times l_{ij} \times e_{0i})$. As example, for a channel width l_{ij} with a volumetric flow rate

q_i of a fracture i, the convective residence time t_i is computed by the following equation:

$$t_i = \frac{L_i e_{0i} l_{ij}}{q_i}$$
(24)

where l_{ij} is the intersected width between two interconnected channels, L_i is the channel length and e_{0i} is the aperture at zero effective normal stress for fracture i.

In order to consider the effect of retardation owing to the change of the morphological void space of a fracture, the convective transit time t_i is corrected by the factor of retardation $R, (= \tau/f(\tau))$ to yield the real transit time considering the effect of the toruosity. The factor of retardation is varied according to the applied effective normal stress level and Fig. 5 is shown how this factor evolve when for the hydraulic behaviour we used $\tau_0 = 0.3$, $\beta = 10.0$ and $q = 1.0$ in Eqn. (2) and $\alpha = 10.0$ and $\gamma = 1.0$ in Eqn. (4)

We assume that because of the effect of longitudinal dispersion along the flow direction, the particle is moved by a effective length $L_i + S a$. Therefore, the effective transit time
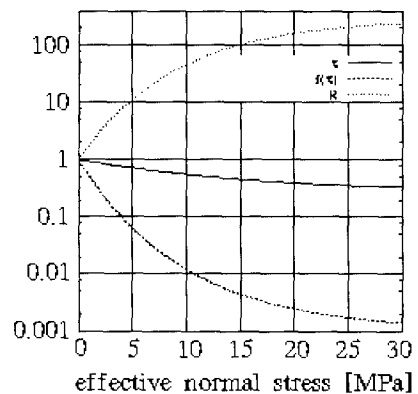

Fig. 5. Relation among τ, $f(\tau)$ and R according to the variation of the effective normal stress.

t_e is inversely proportional to this length and is given by:

$$t_{ei} = t_i \frac{L_i}{L_i + Sa} \tag{25}$$

The reversible linear adsorption is also introduced to represent the retardation along the fracture walls using the surface equilibrium constant K_a (i.e. for the case of non reactive solute, $K_a = 0$) (Moreno et al., 1985). The effective transit time is hence affected from the multicative factor R_f for a fracture element i as follows (Nordqvist et al., 1996):

$$R_f = 1 + \frac{2K_a}{e_{0i}} \tag{26}$$

Finally, the effective transit time t_a involving adsorption effect from t_e is given by:

$$t_{ai} = t_{ei}\left(1 + \frac{2K_a}{e_{0i}} \right) \tag{27}$$

The sum of all the transit times calculated at each channel from the upper boundary to the lower boundary gives the transit time of a particle. By repeating the calculation of a great number of particles, we can obtain a transport breakthrough curve.

This transport model was verified with the data obtained from in situ experiments performed in the geothermal site of Mayet de Montagne (France) (Jeong, 1996).

5. Application to the Soultz sous Forts HDR site

5.1 Description of Geometrical Model for Soultz Site

The Soultz sous Forts HDR site (Fig. 6) is characterized by the existence of the highly conductive dipping faults, related to the regional grabben geological context. In between these

Fig. 6. The geothermal research site of Soultz sous Fort

main features, a dense network with smaller fractures has been identified. Most of them belong to two subvertical sets, respectively striking N170 and N155. For our modelling purpose, we assume that the faults have a large but finite extension. Four of them are introduced in the geological model, as portions of parallel planes (orientation N150 and dip 65W), elliptical shape with about 1 km in vertical direction and about 0.6 km in horizontal direction. Their positions in space were identified by the delineations appearing in plan view of the microseismic locations, monitored in 1993 and 1995 (Baria et al., 1995). The first of these four faults is crosscuting the vertical bore hole GPK 1 at a depth of about 2900 m. Because of its orientation, it passes above and eastward of the top of the open section of the bore hole GPK 2, which extends from –3200 m down to –3800 m. The second is located in the vicinity of GPK 2 at a depth of 3450 m and passes under and westward to the bottom of bore hole GPK 1, which extends from –2800 m down to –3600 m. The third is located at 300 m to the north of the first one, and the forth 300 m to the south of the second one. In reality, none of these faults allows to connect continuously the flow

pathways in between two bore holes. The connectivity of the flow path within this fault system results from the set of individual smaller fractures. We introduced to the two equally dense fracture sets, respectively striking N170 and N150 with a total density of 2.5×10^{-5} fracture center per unit volume of rock mass. These fractures are disc-shaped, with log-normally distributed radii ranging in [12.5 m, 40 m]. The two above distributions (density and size) lead to a mean separation distance between two successive fractures of about 60 m along the vertical bore holes, which is satisfying with regard to the number of flowing joints at the bore holes.

Nevertheless, the resulting fracture network remains rather sparse, with an average number of connections per fracture of 2.7. Assuming that each of the tens of thousands seismic events located in the circulated reservoir is associated with a portion of fracture, it can be anticipated that the porosity of the model will not be in agreement with the in situ porosity. To remediate this apparent bias in porosity, we propose to superimpose to the networks a dense (6.0×10^{-5}) random distribution of the small fractures with 5~15 m in extension.

5.2 Calibration of Flow

In situ evidences are shown the existence of conductive persistent flow path throughout the fracture network, transmitting pressure waves very fast, in a vertical as well as in the north-south direction as identified by GPK 1, EPS 1 and 4616 in synchronism responses to GPK 2 injection test of July 1995. Moreover the fluid produced by GPK 1 during the circulation with reinjection in GPK 2 reveals a rather low temperature of about $135^{\circ}C$, indicating a rapid fluid flow from upper levels towards the top of GPK 1 bore hole. A slowing warming trend was observed, indicating a possible increment of warmer fluid coming from GPK 2 through

Table 1. Parameters used for the three stimulated zones

Bore hole	Depth (m)	$\Delta\Psi$ of stimulation (MPa)	Extention (m)
GPK 1	2,600	9.0	200
GPK 1	3,000	9.0	300
GPK 2	2,500	10.0	200

deeper flow paths.

5.2.1 Description of Parameters Used in Mechanical Properties

As a result of the hydraulic treatments with highly elevated injection rate, the modelled discs belonging to the area delimited by the recorded seismic events are dealt as stimulated. As mentioned in section 2.3, according to a simple criterion depending on a constant stimulation pressure, 0.8 of internal friction angle $\tan(\Phi)$ associated with a zero of cohesion and 3° of angle of dilation are applied. Also 40,000 MPa and 0.25 of Module of Young and Poisson ratio respectively are used. Three stimulated zones are introduced, two of them being connected to the bore hole GPK 1 and the third one in the vicinity of the bore hole GPK 2. Table 1 gives the three hydraulic heads and sizes of stimulated zones.

As far field stress tensor, the principal components at depth of 4,000 m are 54 MPa, 100 MPa and 103 MPa for the minimum horizontal stress, the maximum horizontal stress and the vertical stress respectively. We assume that the maximum horizontal stress is striking in the N170 direction. Stress gradients with depth are fixed at 0.0135 MPam^{-1}, 0.0250 MPam^{-1} and 0.0255 MPam^{-1} for the minor horizontal component, the major horizontal component and the vertical component respectively.

5.2.2 Parameters for Hydraulic Properties

The global configuration in order to calibrate the hydraulic parameters were twofold. Firstly,

the produced flow rate of about 21 ls^{-1} with the corresponding negative hydraulic head of about -2.4 MPa, accounting for buoyancy effect and submerged pump as driving forces and secondly the net reinjected flow rate of about 12 ls^{-1} (already corrected from leaks at the casing shoe) associated to a + 6 MPa hydraulic head. The trial and error matching process combines other constraining observations, mainly flow logs which show that about 70 % of the produced flow rate comes out from the upper part of bore hole GPK 1 while nearly 50 % are reinjected at the bottom part of bore hole GPK 2. The fluid pressure generally declines within 6~12 hours down to the steady-state level. The main features at the steady-state regime between both two bore holes GPK 1 and GPK 2 are listed in Table 2.

Dealing with outer boundary conditions, our knowledge remains poor and this will cause the uncertainties in the hydraulic properties evaluations. We will simulate the fracture networks generated in ablock of fractured rock mass with 0.6 km × 2.0 km × 2.0 km in dimension, elongated in the north-south direction. The bottom of this volume represents the depth -4.0 km and is impervious. Other boundary surfaces are prescribed the hydraulic heads with a constant assigned value of +0.2 MPa.

The result through the matching process is an estimation of the hydraulic aperture of the individual fractures, under zero effective normal stress, which is on the order of 0.625×10^{-3} m and the aperture of the continuous faults which may be twice as thick, on the order of $1.150 \times$

Table 2. Hydraulic heads and flow rates characterizing the steady-state regime of the simulated volume. (∗) At the well head, +6 MPa were recorded for about 20 ls^{-1} of reinjection. Because of the leak off at the GPK 2 casing shoe, only about 12 ls^{-1} were reinjected in the reservoir. This is performed with a lower reinjection hydraulic head.

Driving force	H (GPK 1) (MPa)	H (GPK 2) (MPa)	Q (GPK 1) (ls^{-1})	Q (GPK 2) (ls^{-1})
Buoyancy	-1.2	+0.2	-11.5	-0.6
Buoyancy+Pump	2.4	+0.2	-20.0	-1.1
Buoyancy+Pump+reinjection	-2.4	+3.0	-21.7	-13.1

Table 3. Flow rates, in [ℓ s^{-1}], at each boundary imposed, after reaching at the steady-state regime.
These values are calculated from 10 equally consistent stochastic networks of the simulated reservoir. The negative sign means outflows

Network	Q (GPK 1)	Q (GPK 2)	Q (Top)	Q (south)	Q (north)	Q (west)	Q (east)
1	-22.58	+14.84	+3.89	-1.46	+0.66	+9.20	-4.70
2	-20.80	+12.70	+3.45	-1.44	+0.98	+8.87	-3.92
3	18.97	+13.95	+2.96	-1.34	+0.34	+8.74	-5.63
4	-21.08	+13.42	+3.48	-0.84	+0.63	+9.86	5.57
5	-17.80	+13.33	+3.04	-1.30	+1.14	+7.39	-5.57
6	-20.52	+16.97	+3.53	-2.23	+0.91	+7.85	6.29
7	18.43	+12.04	+3.03	-1.19	+0.72	+8.53	4.75
8	-19.14	+12.55	+3.25	1.23	+0.88	+7.69	-4.25
9	-18.93	+15.03	+3.59	-1.98	+1.08	+6.88	-5.56
10	21.75	+13.06	+3.20	-1.35	+0.95	+9.77	4.00
Mean	-20.05	+13.80	+3.35	-1.43	+0.83	+8.85	-5.02

10^{-3} m. The non linear flow rules producing the transient behaviour are the exponential relationships between the aperture and the effective normal stress as mentioned in section 2.2. They are given by two empirical expressions as follows:

$$\tau = 0.35 + 0.65\exp\left[-\left(\frac{\sigma'}{15.0}\right)^1\right] \qquad (28)$$

$$f(\tau) = \exp[-8.0(1-\tau)^1] \qquad (29)$$

Table 3 contains the mean values for the calculated flow rates at the bore holes in various conditions with 10 equiprobable network. The adopted sign convention is a negative value for fluid leaving the fracture system. These mean flow rates for two bore holes GPK 1 and GPK 2 are satisfying when compared with those in Table 2.

The quasi stationary hydraulic regime is reached after about 5 days as illustrated in Fig. 7. It is noticeable that both bore holes behave rather independently in spite of the extensive stimulation efforts, so that the pure contribution of reinjected fluid to the production bore hole remains to about $3\sim5$ $\ell\,s^{-1}$.
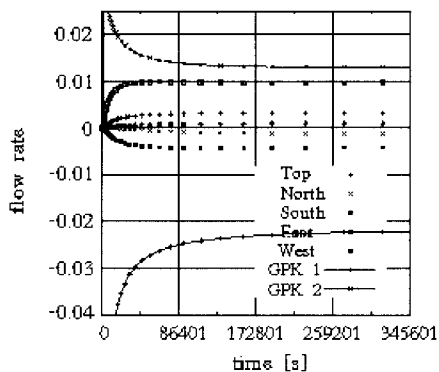
5.3 Transport Simulation between Two Bore holes, GPK 1 and GPK 2

We simulate the transport of non reactive particles through the 10 equiprobable networks used for the flow calibration, after reached at the steady-state regime between upstream and downstream boundaries. 100,000 particles are individually introduced in bore hole GPK 2 and the transit time of each particle is calculated. An example is given by Fig. 8 which shows a
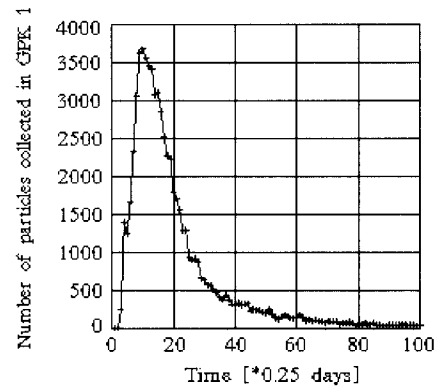

Fig. 8. A simulated breakthrough curve, with a reinjection rate of 13.1 $\ell\,s^{-1}$ and a production rate of 21.7 $\ell\,s^{-1}$

Fig. 7. Flow rates versus time through the boundaries imposed for one particular realization of the 10 network.
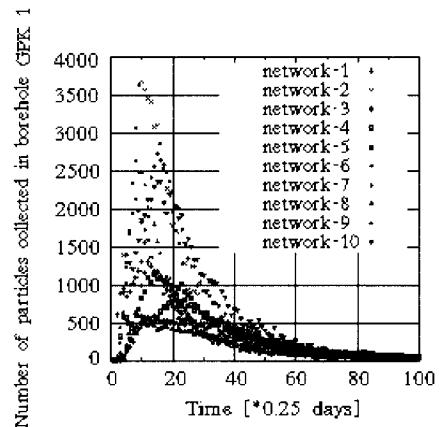

Fig. 9. Ten simulated breakthrough curves, corresponding to ten equiprobable networks

sharp breakthrough curve corresponding to a calculated mass recovery factor of about 60 %.

These calculations are repeated for 10 equally consistent fracture networks which are the same as when the flow calibration is performed in previous section. We obtained 10 breakthrough curves (Fig. 9) and the mean transit time is of the order of one week for a non reactive tracer element between the two bore holes GPK 1 and GPK 2.

6. Conclusion

The aim of this work was to propose the transport model which is simple and adapted to represent the phenomenon of the tracer dispersion in the fractured medium where is subjected to the forced circulation of a fluid and the far field stress. To do so, we used a particle transport model, that is particle following that the main parameter is concerned with the fracture behaviour model which is coupled hydraulic model and mechanical model.

The result obtained from numerical simulations for transport bahaviour prediction between two deep bore holes from the experimental data sets of Soultz sous Fort geothermal research site, shows that the mean transit time for a non reactive solute is about one week in the actual situation of this fractured reservoir and in the forced circulating regime of about 20 ℓ s^1.

Since no tracer test is yet available at this geothermal site but is in progress, the actual transit time between the two bore hole GPK 1 and GPK 2 is still unknown. In this paper, we presented revised estimates of breakthrough curves and mean transit time, for the hydraulic regime that has already been investigated.

Notations

β : empirical constant   (MPa)

μ : dynamic viscosity

ν : Poisson ratio   (kg/(m s))

ρ : fluid density   (kg/m^3)

σ : normal loading stress   (MPa)

σ' : effective normal stress   (MPa)

Φ : internal friction angle

Ψ : fluid pressure   (MPa)

C : cohesion   (MPa)

d_i : bond length in fracture i (m)

E : Young's modulus   (MPa)

e_0 : aperure at zero effective normal stress   (m)

g : gravitational acceleration   (m s^{-2})

k_0 : reference hydraulic conductivity at zero effective normal stress   (m^3 s^{-1})

K_a : surface equilibrium coefficient

l : width of half bond   (m)

q : empirical shape factor

Q_i : local flux in fracture i (m^3 s^{-1})

R : fracture element radius   (m)

R_f : retardation factor

S : standard deviation

Δt : time interval

t_i : convective transit time   (s)

t_e : effective transit time   (s)

t_a : effective transit time under consideration of retardation   (s)

Δu : slip displacement   (m)

Reference

Andersson, J. and Dverstorp, B. (1987). "Conditional simulations of fluid flow in three-dimensional networks of discrete fractures." *Water Resour. Res.*, Vol. 23, No. 10, pp. 1896-1886.

Baecher, G.B., Lanney, N.A. and Einstein, H.H. (1977). "Statistical description of rock properties and sampling." *Proceedings of the 18th U.S. Symposium on Rock Mechanics*, American Institute of Mining Engineers –

5C1-8.

Bruel, D., Cacas, M.C., Ledoux, E. and de Marsily, G. (1994). "Modelling storage behaviour in a fractured rock mass." *Journal of Hydrology*, Vol. 162, pp. 267-278.

Cacas, M. C., Ledoux, E., de Marsily, G., Tillie, B., Barbreau, A., Durand, E., Feuga, P. and Peaudecerf, P. (1990). "Modelling fracture flow with a discrete fracture network: calibration and validation. 1. The flow model." *Water Resour. Res.*, Vol. 26, No. 3, pp. 479-489.

Ciarlet, P. (1983). "Introduction l'analyse numrique matriciel et l'optimation." *Masson.*

Ezzedine, S. (1984). *Modlisation des coulements et du transport dans les milieux fissurs.* These de Doctorat de l'Ecole des Mines de Paris.

Gale, J.E. (1982). "Assessing the permeability characteristics of fractured rock." *Recent Trends in Hydrogeology*, Edited by Narasimhan, T.N., Geological Society of America, Special Paper 189, pp. 163-181.

Gale, J.E., Rouleau, A. and Atkinson, L.C. (1985). "Hydraulic properties of fracture." *Congress International Association of Hydrogeologists*, Vol. 17, pp. 1-11.

Gentier, S. (1986). *Morphologie et comportement hydromcanique d'une fracture naturelle dans un granite sous contrainte normale. Etude exprimentale et thorique.* These de Doctorat de l'Universit d'Orleans.

Huyakorn, P.S. and Pinder, G.F. (1983). *Computational methods in subsurface flow.* Academic, New York.

Jeong, W.C. (1996). *Modlisation probabilistic discrete d'un milieu fissur: Evaluation des performances hydrauliques d'un doublet gothermique pilote dvelopp grande profondeur dans le foss Rhnan.* Mmoire de DEA de l'Ecole des Mines de Paris.

Moreno, L., Neretnieks, I. and Eriksen, T. (1985). "Analysis of some laboratory tracer runs in natural fissure." *Water Resour. Res.*, Vol. 21, No. 7, pp. 951-958.

Moreno, L., Tsang, Y.W., Tsang, C.F., Hale, F.V. and Neretnieks, I. (1988). "Flow and transport in a single fracture a stochastic model and its relation to some field observation." *Water Resour. Res.*, Vol. 24, No. 12, pp. 2033-2048.

Nordqvist, A.W., Tsang, Y.W., Tsang, C.F., Dverstrop, B. and Andersson, J. (1992). "A variable aperture fracture network model for flow and transport in fractured rocks." *Water Resour. Res.*, Vol. 27, No. 12, pp. 1703-1713.

Nordqvist, A.W., Tsang, Y.W., Tsang, C.F., Dverstrop, B. and Andersson, J. (1996). "Effects of high variance of fracture transmissivity on transport and sorption at different sacles in a discrete model for fractured rocks." *Journal of Contaminant Hydrology*, Vol. 22, pp. 39-66.

Raven, K.B. and Gale, J.E. (1985). "Water flow in a natural rock fracture as a function of stress and sample size." *International Jointed Rock Mechanics, Mining Science and Geomechanics.* Vol. 22, No. 4, pp. 251-261.

Tsang, Y.W. and Tsang, C.F. (1987). "Channel model of flow through fractured media." *Water Resour. Res.*, Vol. 23, pp. 467-479.

Tsang, Y.W., Tsang, C.F., Neretniecks, I. and Moreno, L. (1988). "Flow and tracer transport in fractured media: A variable aperture channel model and its properties." *Water Resour. Res.* Vol. 24, No. 12, pp. 2049-2060.

<최종본 접수일 : 1998년 5월 13일>